Hindawi
Geofluids
Volume 2022, Article ID 6534034, 17 pages
https://doi.org/10.1155/2022/6534034

Research Article

Particle Flow Analysis of Acoustic Emission Features of Rock under Rock Burst Stress Path

Yalei Wang and Jinming Xu

Department of Civil Engineering, Shanghai University, Shanghai 200444, China

Correspondence should be addressed to Jinming Xu; xjming211@163.com

Received 23 August 2022; Revised 23 October 2022; Accepted 3 November 2022; Published 19 November 2022

Academic Editor: Yuanyuan Zha

The AE (acoustic emission) features could reflect the process of fracture initiation and propagation in rocks. Taking Lalin railway tunnel granite as an example, a three-dimensional particle flow numerical model of rock was established based on the PFC (particle flow code). The mechanical properties between particles were simulated using parallel bond. The rock burst stress path was simulated using the movement of the wall in the particle flow model. The results of uniaxial compression tests in a laboratory were used to calibrate the mesoscale mechanical parameters of the particle flow model. AE features of rock deformation and failure under different confining pressures were then studied. It shows that the unloading direction of rock may produce strong dilatation deformation during rock burst; with the increase of confining pressure, the more obvious dilatation deformation and the more possibility of serious rock burst to occur; the unloading failure of rock reveals that rock burst is a mixed failure of tensile and shear, and the tensile cracks account for about 70%; the number of AE events of rock unloading failure occur at the top and bottom of the rock first and then expand rapidly to the middle part until the rock is completely destroyed; in the process of rock burst, AE rupture strength is relatively concentrated, the number of AE events surge obviously, and the number of AE events in surge period account for more than 80% of all AE events. The results presented herein may be referable in analyzing the mechanism of rock burst.

1. Introduction

The occurrence of rock burst is closely related to the initiation and propagation of cracks in rocks. AE (acoustic emission) activities could reflect the porosity of rock, according to Ma et al. [1], the development of cracks in rocks as well [2], and provide important reference value for the early warning of rock burst in construction. At present, there are many researches on the mechanism of rock burst using AE features in the process of rock fracture. For example, Li et al. [3] analyzed the relationship between rock burst tendency and AE features through uniaxial compression test; Tian et al. [4], respectively, studied the variation rules of AE events in granite, marble, and basalt during rock burst tests; Zhang et al. [5] divided rock burst into three stages using the AE dominant frequency features of granite in the failure process of biaxial loading; Su et al. [6] conducted unloading failure test on granite by true triaxial test equipment, and discussed the precursor of rock burst failure using AE ringing count and b value; Pei et al. [7] conducted uniaxial cyclic loading and unloading tests on granite, revealing the AE features of rocks with different rock burst tendencies in the failure process; Zhai et al. [8] used AE technique to analyze the fracture evolution of granite and basalt in the process of rock burst fracture; Chu et al. [9] conducted the uniaxial compression rock burst test of granite in deep tunnel and discussed the variation rule of AE features in combination with mechanical properties; Wang et al. [10] proposed a multiparameter collaborative rock burst estimation method using comprehensive analysis of AE energy and dominant frequency entropy; Tan et al. [11] discussed rock burst failure mechanism based on AE features of anchored sandstone during uniaxial compression failure process; Wang et al. [12] explored the variation features of

AE energy and event number of rocks with different rock burst tendencies during uniaxial compression deformation and failure.

At the same time, PFC (particle flow code) has been widely used in geotechnical engineering in recent years because it could well simulate the fracture of bonding between particles under external force. For example, Zhou et al. [13] and Cai et al. [14] used PFC method to analyze the variation rules of AE event location and fracture strength in the process of rock deformation and failure under uniaxial compression; Zhang et al. [15] conducted numerical simulation of biaxial compression test of granite by using PFC and analyzed the relationship between loading rate and AE events; Wang et al. [16] analyzed the difference of AE energy between tensile fracture and shear fracture of sandstone by using PFC method; Wang et al. [17] researched the mechanical properties and AE features of rock by using PFC method and discussed the damage evolution law of rock based on the AE features; Liu et al. [18] established the numerical model of coal-rock combination by using PFC and studied the influence of different height ratios on the AE features of the coal-rock combination; Gao et al. [19] studied the AE features of coal specimens during loading and unloading failure and explored the influence of periodic load on the AE count; Liu et al. [20] established rock particle flow models at different scales based on PFC method, and discussed damage evolution rules using AE features; based on PFC method, Feng et al. [21] considered the relationship between AE features and failure modes of jointed rocks with different dip angles under uniaxial compression; Hu et al. [22] used PFC method to conduct numerical simulation analysis of rock burst and then analyzed the initiation and expansion rules of fractures.

To sum up, AE is an intuitive representation of rock fracture. The AE activities could describe the details of rocks in deformation and failure processes. AE features could be used to characterize the fracture and instability process of rocks as well. However, the above studies mostly focus on the variation rules of AE features in the process of rock loading and unloading and often ignore the influence of the rock burst stress path and confining pressure on AE features in rocks. Therefore, the uniaxial compression test of granite in Lalin railway tunnel was conducted. The three-dimensional particle flow model of rock was established based on PFC^{3D} and the results of the uniaxial compression test. The stress path of tunnel wall rock burst was simulated. AE features in the process of rock deformation and failure under different confining pressures were studied, and the mechanism of rock burst was then explored.

2. Establishment of Three-Dimensional Particle Flow Model for Rock

2.1. Rock Burst Features of Tunnel Where Rock Specimen Is Located. Rock specimen was taken from the Bayu Tunnel along the Larin Railway in western China. Bayu Tunnel is located in the lower Sangri-Gacha section of southern Tibet, close to the southern bank of the Yarlung Zangbo River, with steep terrain. The natural slope of the entrance section is 45°~75°, the natural slope of the exit section is 45°~55°, the maximum buried depth is 2080 m, and the ground elevation of the tunnel site is 3260~5500 m. It belongs to the typical appearance of a mountain canyon. The bedrock lithology is mainly diorite and granite, and the geological structure is complex.

Table 1: Results of rock uniaxial compression test.

Location	Macroscopic mechanical parameter		
	E_0 (GPa)	ν_0	σ_{f0} (MPa)
DK194 + 200.2	4.86	0.23	55.99

Table 2: Geometric parameters of particle flow model.

Dimensions of model		Dimensions of particles	
Radius (mm)	Height (mm)	R_{min} (mm)	R_{max}/R_{min}
25	100	1.0	1.66

The Bayu Tunnel was dominated by medium and strong rock burst. The rock specimen was located at DK194 + 200.2 of the Bayu Tunnel, with a buried depth of 1446.1 m and high in situ stress (maximum principal stress is 49.7 MPa). During the rock burst, flakes of stone fell from the top left of the roof (facing the palm), and then a strong cracking sound was heard. A large number of large rocks are rapidly ejected from the top and wall of the tunnel, and the thickness of the rocks reached more than 30 centimeters. The rock powder injection phenomenon is serious in the construction site, and the rock burst pit is continuously distributed, and the maximum depth of the pit is more than 2 meters. Using the code for hydropower engineering geological investigation (suggested by the National Standards Compilation Group of People's Republic of China [23]), the rock burst grade was determined at the strong level.

2.2. Calibration of Microscopic Mechanical Parameters. Taking granite at DK194 + 200.2 of Lalin railway tunnel as an example, the cylindrical specimen in a diameter of 50 mm with a height of 100 mm was made from the field core. A particle flow model of rock was established based on PFC^{3D}, and the microscopic mechanical properties of the particle flow model were calibrated using the results of indoor uniaxial compression test. The indoor uniaxial compression test results are shown in Table 1. In Table 1, E_0, ν_0, and σ_{f0} represent elasticity modulus, Poisson's ratio, and peak stress, respectively.

The geometric size of the particle flow model needs to be consistent with the appearance size of the specimen. The geometric parameters of the particle flow model are shown in Table 2. In Table 2, R_{max} and R_{min} represent the maximum and minimum radius of the particles in the particle flow model, respectively.

In the process of initial model establishment, three walls were established based on the appearance size of the specimen, including a cylindrical wall labeled 3 to simulate the loading and unloading of confining pressure, and two plane walls were labeled 1 and 2 to simulate the bottom plate and

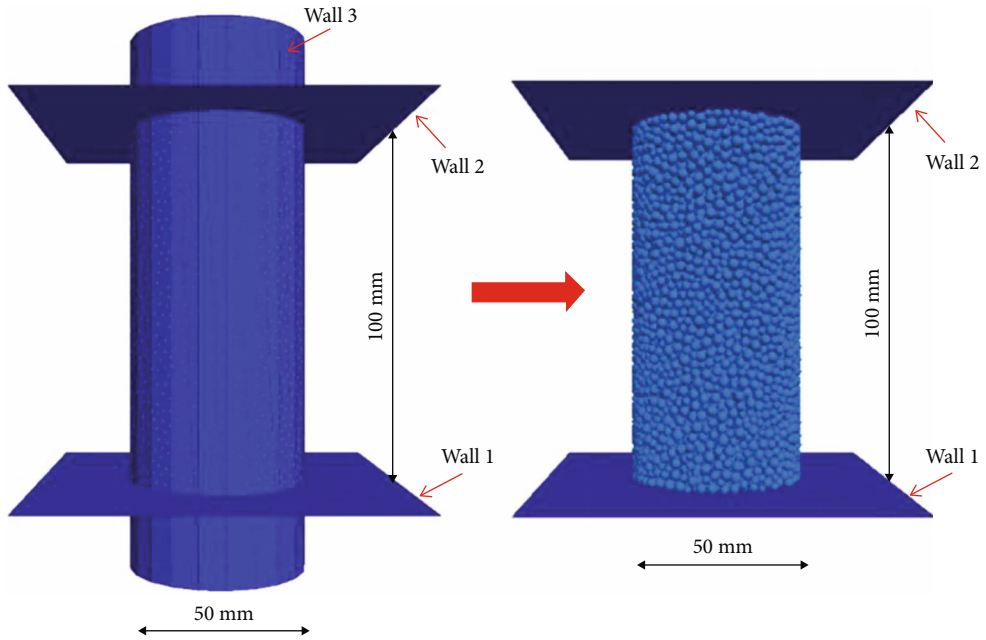

Figure 1: Particle flow model of rock under uniaxial compression.

top plate of the test loading equipment, respectively. According to R_{min} and R_{max}/R_{min}, particles were randomly generated in the enclosed space surrounded by the three walls. By controlling the position of the walls, the stress between particles was released and the equilibrium state was reached. About 11541 balls and 39154 contacts were generated to form the initial model of rock particle flow. The simulation needs to call the initial model first, and then perform other operations to ensure that all subsequent simulations were carried out under the same initial model conditions so as to avoid the influence of particle distribution difference on the simulation results in the process of particle regeneration. Wall 3 was deleted to obtain a particle flow model of rock under uniaxial compression load, as shown in Figure 1.

According to the actual weight and volume of the 6 specimens, the density of the rock was calculated to be 2806 kg/m^3. There are two main kinds of contact models to describe the cementation state inside rock, one is contact bond model and the other is parallel bond model. The contact bond model could only transmit force but not moment, while the parallel bond model could transmit force and moment, which is more suitable for simulating the cementing material between mineral components in rocks. After the particle flow model is loaded, the particles move relative to each other, resulting in force and moment. The force and moment act on the particles, and when the tensile or shear force exceeds the corresponding bond strength, the parallel bond breaks and is transformed into the contact bond model. The parallel bond model is shown in Figure 2.

As shown in Figure 2, when the parallel bond fails and the load could not be transferred, the parallel bond model degenerates to the contact bond model. Parallel bond contains five important mechanical parameters: parallel bond normal strength σ_{pbc}, parallel bond shear strength σ_{pbt}, parallel bond normal stiffness k_{pn}, parallel bond shear stiffness k_{ps}, and contact radius R. These parameters could characterize the total contact force and total contact moment of the bond mode as well. The type of cracks generated by the parallel bond model was controlled by the preset bond parameters. When the maximum tensile stress exceeded the parallel bond tensile strength, a tensile crack was generated; meanwhile, when the maximum shear stress exceeded the parallel bond shear strength, a shear crack was generated. The parallel bond is similar to the weak structural planes that naturally exist in rocks.

Accordingly, the parallel bond was used to describe the contact between particles. The maximum axial stress in the deformation and failure process of rock particle flow model under uniaxial compression was taken as the peak stress σ_{f1}. Poisson's ratio ν_1 was calculated using the ratio of radical strain and axial strain when the axial stress reaches 0.8 times the peak stress. The elastic modulus E_1 was calculated using the axial stress-strain curve. Considering that the relationship of macro- and mesoscopic mechanical parameters [24], the calibration process of microscopic mechanical parameters is as follows:

(1) *Calibration of Elastic Modulus.* The parallel bond normal strength σ_{pbc} and parallel bond shear strength $\sigma_{pb\tau}$ were temporarily set to the peak stress (55.99 MPa); the standard deviation σ_{std} of parallel bond normal strength and the standard deviation τ_{std} of parallel bond shear strength were temporarily set to 0; the particle stiffness ratio k_n/k_s was 2.5; the parallel bond stiffness ratio k_{pn}/k_{ps} was 2.5; the parallel bond space g_{ap} was set to 0.07 mm; the parallel bond radius factor f_{pbr} was 1.0; the porosity f_{por} of

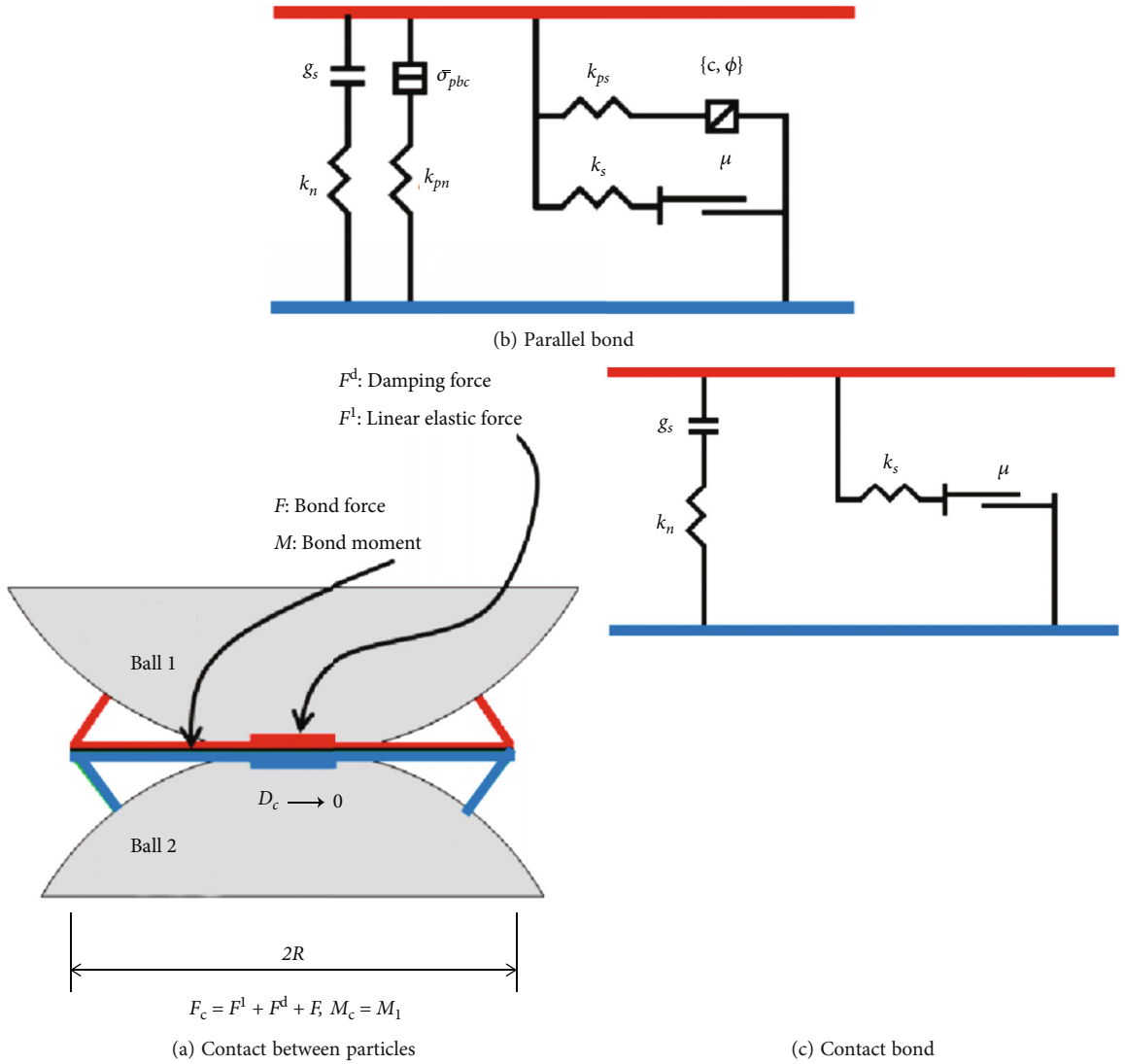

Figure 2: Parallel bond model.

the particle flow model was set to 0.32; the particle friction coefficient μ was 0.5; the minimum radius of the particles was 1.0 mm, while the ratio of the maximum radius to the minimum radius of particles was 1.66; the elastic modulus E_{pb} of parallel bond and the elastic modulus E_p of particles were kept the same. According to the linear correlation between the elastic modulus E_1 of the rock particle flow model and E_p, the value (5.59 GPa) of E_p was selected

(2) *Poisson's Ratio Calibration*. The elastic modulus of particles and the elastic modulus of parallel bonds were both set as 5.59 GPa, and other parameters remain unchanged. According to the linear correlation between Poisson's ratio ν_1 of the rock particle flow model and the parallel bond stiffness ratio k_{pn}/k_{ps}, the value (0.22) of k_{pn}/k_{ps} was selected

Table 3: Parallel bond parameters of the particle flow model.

Parallel bond parameters							
E_{pb} (GPa)	k_{pn}/k_{ps}	σ_{pbc}	σ_{std}	σ_{pbt}	τ_{std}	f_{pbr}	g_{ap} (mm)
4.6	2.0	39.0	5.0	35.0	5.0	5.0	0.07

Table 4: Particle mechanical parameters of the particle flow model.

Particle mechanical parameters						
E_p (GPa)	k_n/k_s	μ	f_{por}	ρ (kg/m^3)	R_{min} (mm)	R_{max}/R_{min}
4.6	2.0	0.5	0.32	2806	1.0	1.66

(3) *Peak Stress Calibration*. The values of E_p and E_{pb} were both set as 5.59 GPa. The value of k_{pn}/k_{ps} was set as 2.2. The parallel bond normal strength σ_{pbc}

Table 5: Comparison between simulation values and actual values.

Location		Macroscopic mechanical parameters		
		Modulus of elasticity (GPa)	Poisson's ratio	Peak stress (MPa)
DK194 + 200.2	Actual values	4.86	0.23	55.99
	Simulation values	4.68	0.23	56.25

and parallel bond shear strength σ_{pbt} were kept equal. According to the linear correlation between σ_{pbc} and the peak stress of the particle flow model, the value (42.40 MPa) of σ_{pbc} was selected. At this time, the elastic modulus of particles, elastic modulus of parallel bond, parallel bond stiffness ratio, parallel bond normal strength, and parallel bond shear strength were, respectively, 5.59GPa, 5.59GPa, 2.2, 42.40 MPa, and 42.40 MPa, and other parameters remained unchanged. Accordingly, the calculated elastic modulus, Poisson's ratio and peak stress of the rock particle flow model were 5.18 GPa, 0.24, and 56.35 MPa, respectively. Obviously, the macroscopic mechanical parameters of the particle flow model are basically close to the test results of rock and only need fine tuning

(4) *Fine Tuning of Parameters*. The standard deviation σ_{std} of parallel bond normal strength and the standard deviation τ_{std} of parallel bond shear strength were added to consider the heterogeneity of the rock, and σ_{std} and τ_{std} were both set to 5 MPa. Micromechanical parameters were repeatedly fine-tuned to reduce the error between the rock particle flow model and rock macromechanical parameters. According to the above methods, the mesomechanical parameters of in the rock particle flow model are shown in Tables 3 and 4

The simulation results of macroscopic mechanical parameters of the rock particle flow model under uniaxial compression load were compared with the experimental results, as shown in Table 5.

As can be seen from Table 5, the difference between the actual and the simulated values of macroscopic mechanical parameters of rock is relatively small. Figure 3 shows the stress-strain curves of rock specimen in the laboratory test and simulation test.

As shown in Figure 4, the numerical simulation test curve is basically consistent with the indoor test curve. In conclusion, the mesomechanical parameters of the particle flow model obtained from this calibration could be used as the basic values of the mesomechanical parameters of the rock specimen.

2.3. Rock Burst Stress Path Simulation. The excavation of the tunnel breaks the original stress balance state of rock mass so that the confining pressure of rock mass decreases rapidly and the axial pressure increases sharply. At this time, the stress state of rock mass is similar to the stress state of axial stress increase under the condition of no confining pressure or low confining pressure. Therefore, the stress path of rock burst in tunnel construction could be simulated by unloading confining pressure and increasing axial pressure. The stress path of the particle flow model is shown in Figure 5.

As shown in Figure 6, the stress path of the particle flow model could be divided into four stages: I, II, III, and IV, corresponding to the stages of confining pressure application, axial pressure application, axial pressure increase while unloading confining pressure, and failure, respectively.

Stage I. Applying confining pressure σ_W to design confining pressure σ_{SW} with displacement control method

Stage II. σ_{SW} was kept unchanged and the axial compression σ_Z was increased to 80% of the peak strength σ_{f1} under uniaxial compression to simulate the accumulation process of rock strain energy

Stage III. Unloading confining pressure while continuing to increase axial pressure to simulate the change of surrounding rock stress state during rock burst

Stage IV. The axial stress dropped rapidly and the specimen failed

3. Acoustic Emission Features of Rock under Different Confining Pressures

According to the above rock burst stress path simulation method, 10, 20, 30, and 40 MPa were selected as the confining pressures of the rock particle flow model, respectively. Axial loading speed was set as 0.2 m/s during confining pressure unloading. Axial or radial strain is positive in compression and negative in tension. The volumetric strain is positive in shrinkage and negative in dilation. Figure 3 shows the stress-strain curves of the rock particle flow model in the process of deformation and failure under different confining pressures.

As shown in Figure 3, with the increase of confining pressure, the peak strength of rock during unloading failure increases to a certain extent. In the axial pressure application stage, the axial compression strain is much larger than the radial expansion strain. At this time, the rock volumetric strain is mainly compression and the strain energy is accumulated; in the axial pressure increases while unloading confining pressure stage, the radial dilating strain increases quickly and the volumetric strain changes rapidly from compression to expansion. The expansion velocity of radial strain and the transformation velocity of volumetric strain from compression to expansion increase with the increase of confining pressure; in the failure stage, the axial stress decreases rapidly, the radial strain expansion rate is greater than the axial strain compression rate, and the volumetric strain is mainly dilated; with the increase of confining pressure, the dilatation of rock during unloading failure

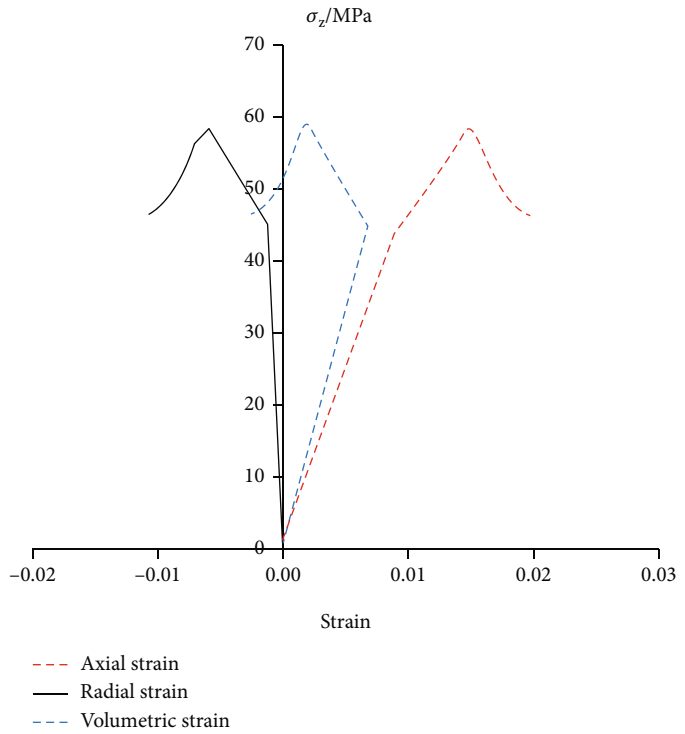

(a) 10 MPa

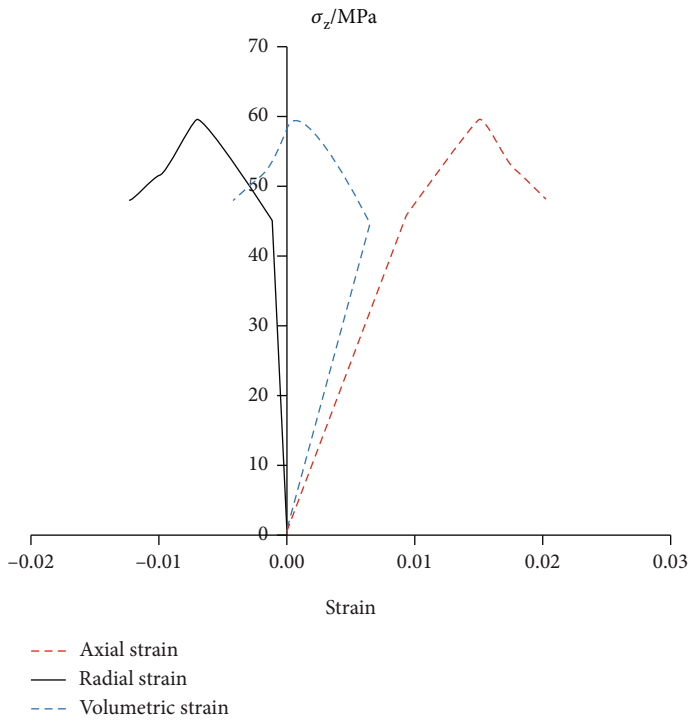

(b) 20 MPa

Figure 3: Continued.

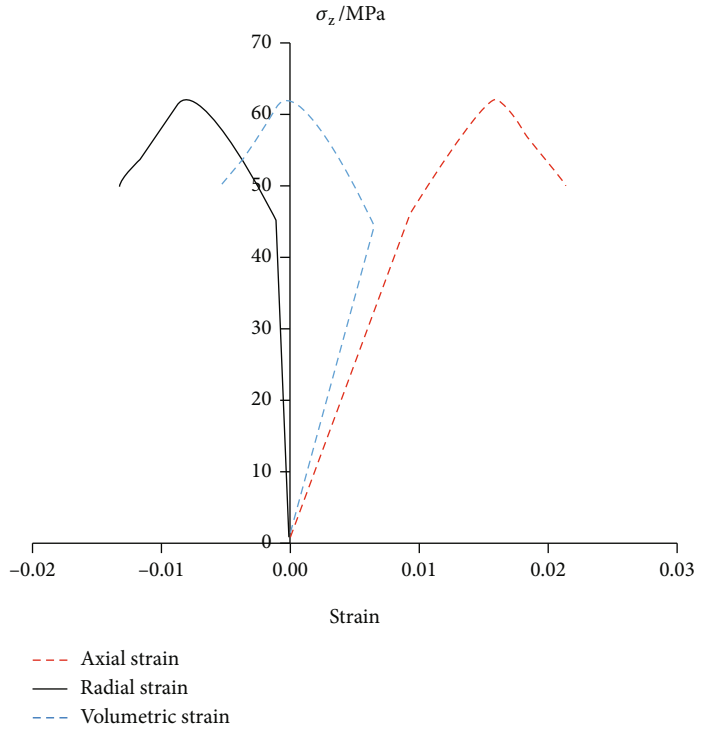

(c) 30 MPa

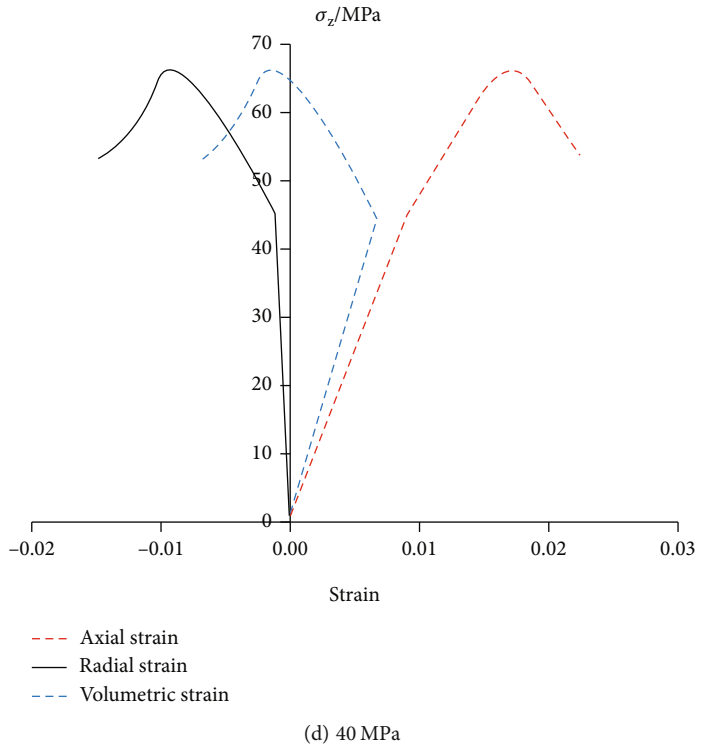

(d) 40 MPa

Figure 3: Stress-strain curves under different confining pressures.

increases obviously, indicating that the greater the horizontal tectonic in situ stress of surrounding rock, the stronger the dilatation of surrounding rock during tunnel excavation, and the higher the possibility of rock burst.

Considering that the rock burst process is a strong expansion deformation phenomenon of tunnel wall caused by tunnel excavation activities, the rapid expansion of volume strain in the process of rock mass unloading failure caused by tunnel activities in a high stress area was easy to evolve into surrounding rock burst failure. The AE features of the rock particle flow model in the process of unloading failure under different confining pressures were then

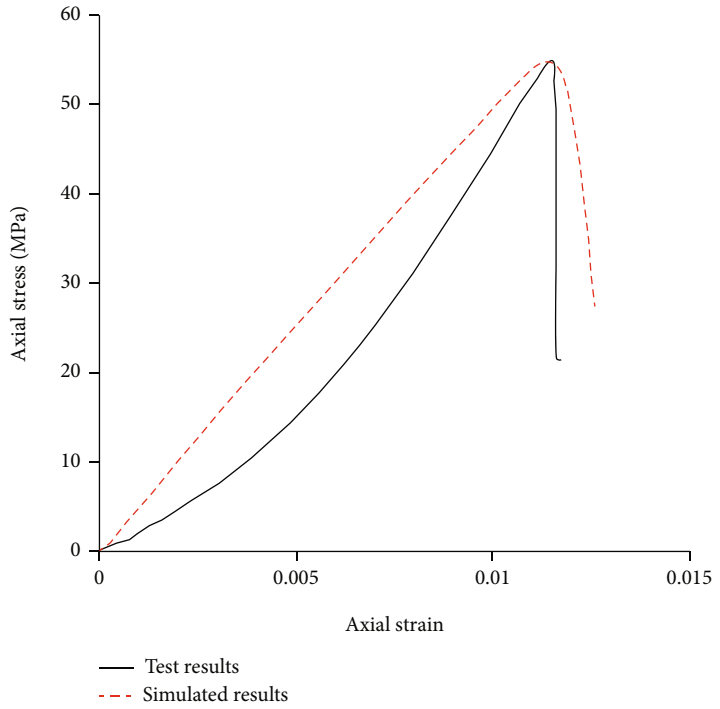

Figure 4: Comparison of stress-strain curves.

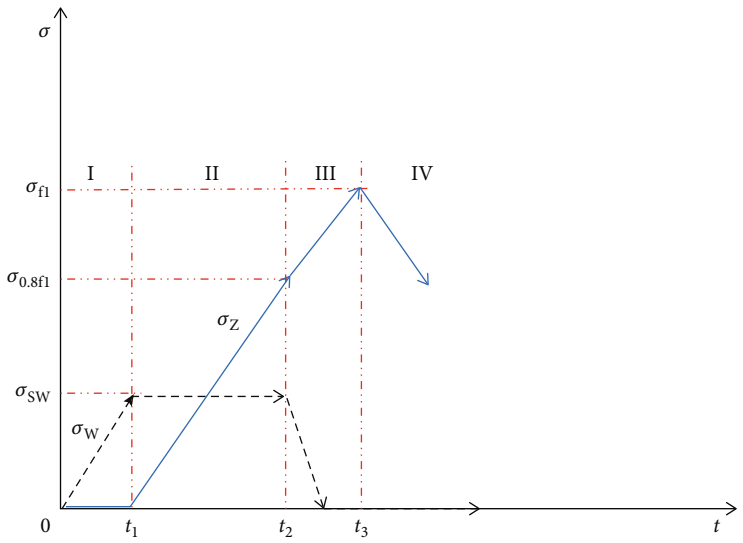

Figure 5: The stress path of particle flow model.

analyzed. The relationship between the number of AE events and stress-strain during rock fracture is shown in Figure 6.

As shown in Figure 6, before the axial stress of rock is loaded to 0.8 times of peak stress, AE activities are very calm and few AE events occur; for the case of low confining pressure (10, 20 MPa), the AE events mainly occur after the confining pressure is completely unloaded. At this time, the stress state of rock is close to uniaxial compression deformation failure; for the case of high confining pressure (30, 40 MPa), the AE events mainly occur before the confining pressure has completed unloading, and the stress state is close to triaxial compression deformation failure; the larger the confining pressure, the more forward the time of a large number of AE events in the rock. At this time, the phenomenon of a large number of AE events in the rock may be regarded as the precursor of rock failure. Therefore, in the process of tunnel rock mass excavation in a high stress area, a large number of cracks and AE events may have occurred in the surrounding rock before the confining pressure is completely unloaded. If the confining pressure is large enough, a large number of cracks may occur in the tunnel rock face and rock burst may occur even if the rock mass is slightly disturbed by tunnel excavation. The surge of AE events before complete unloading may be considered as a

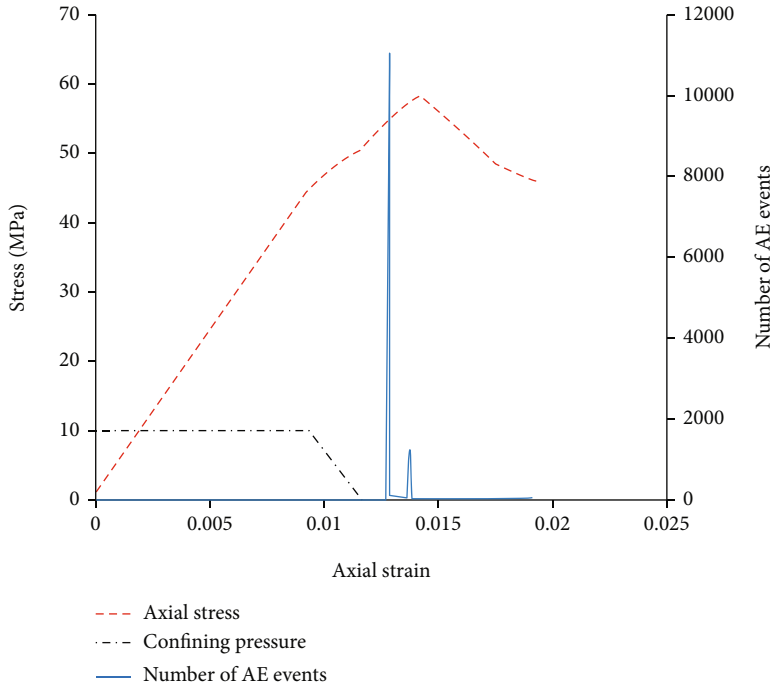

(a) 10 MPa

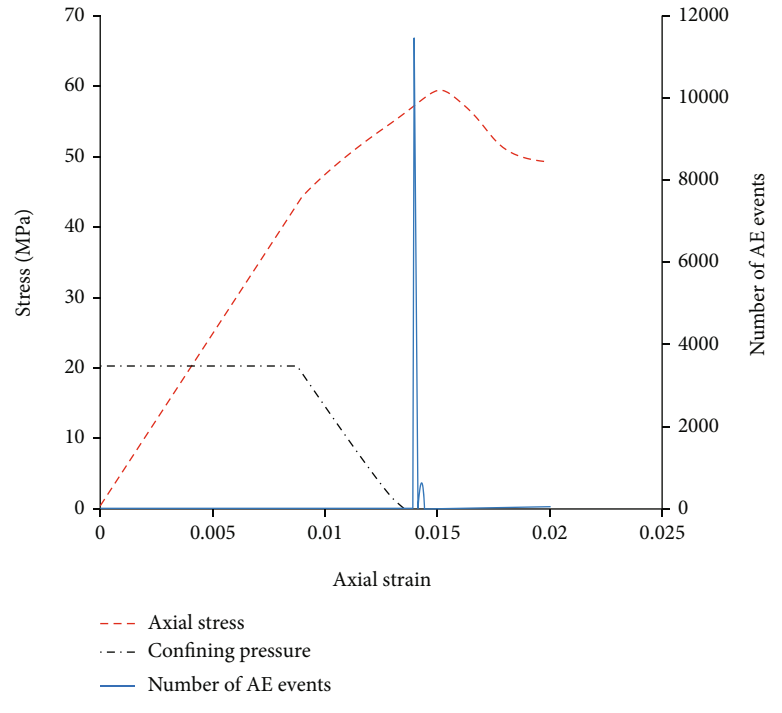

(b) 20 MPa

Figure 6: Continued.

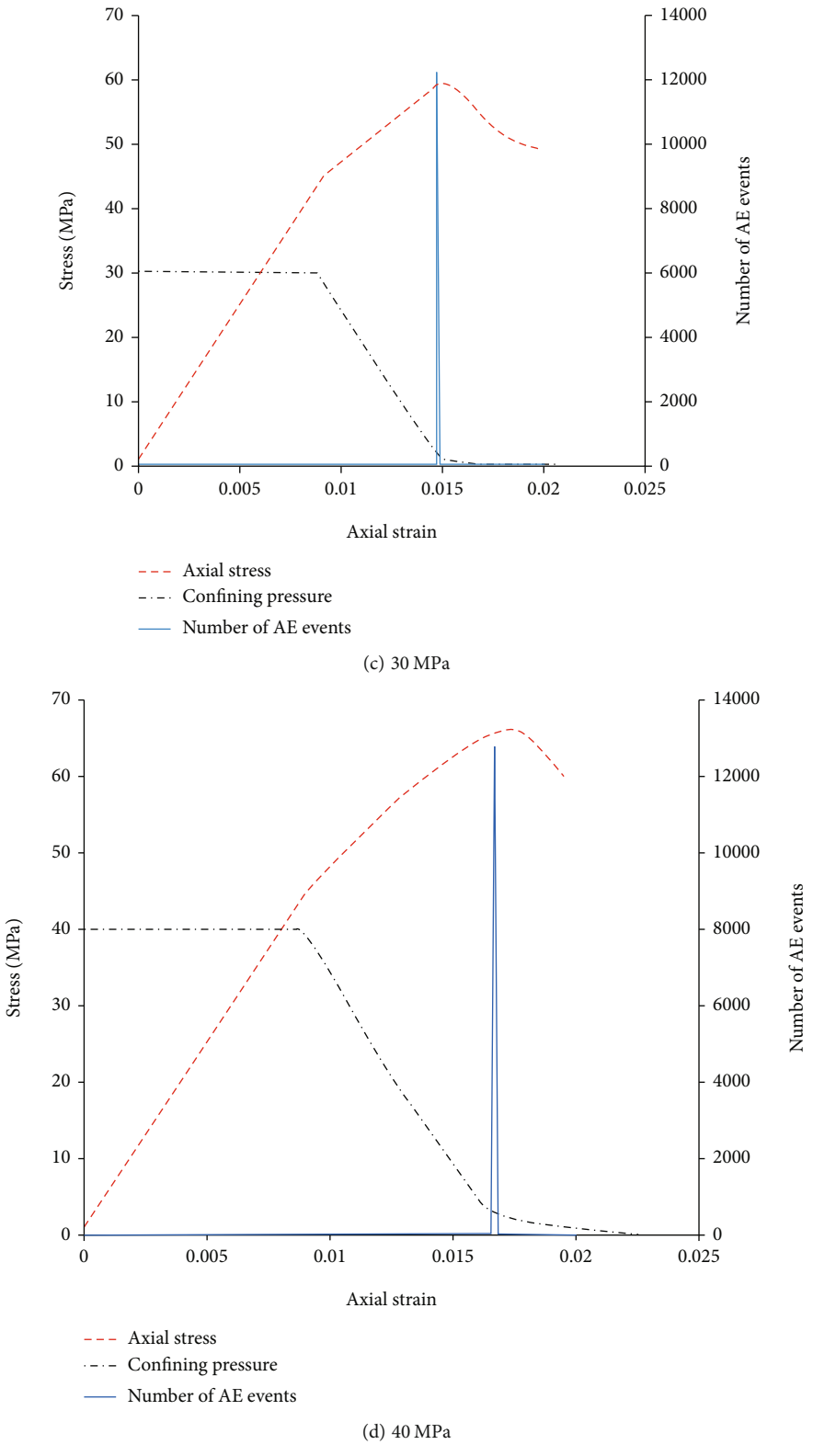

(c) 30 MPa

(d) 40 MPa

Figure 6: Relationship between AE events and axial stress under different confining pressure.

rock burst warning. Rock burst in a high stress area usually occurs before confining pressure is completely unloaded. The greater the confining pressure, the earlier the occurrence time of rock burst and the more sudden it is.

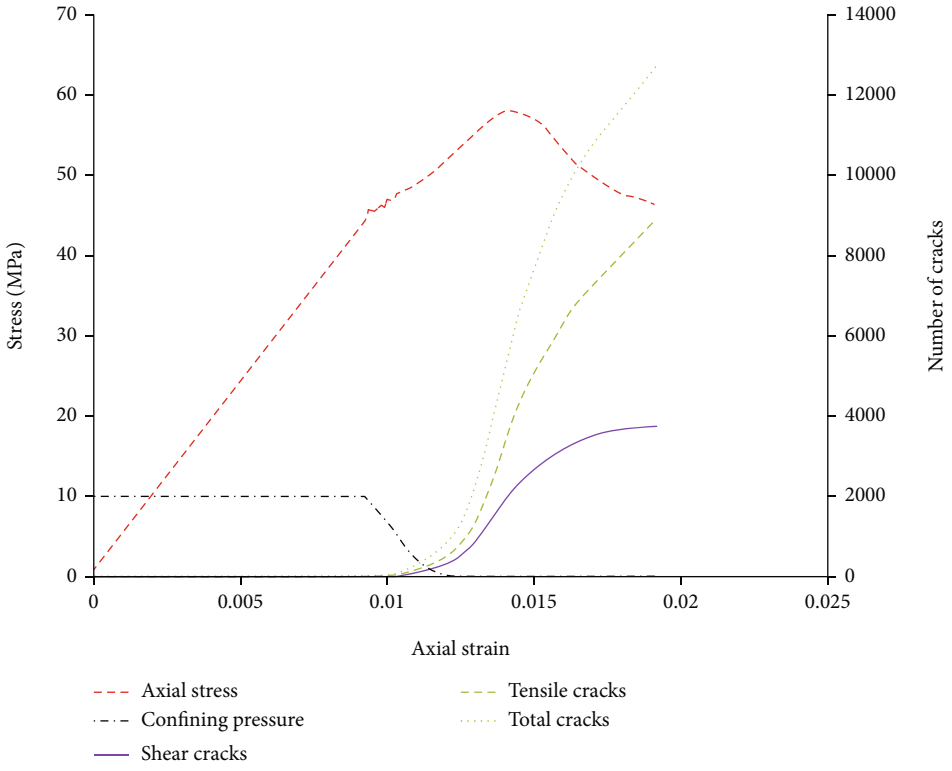

(a) 10 MPa

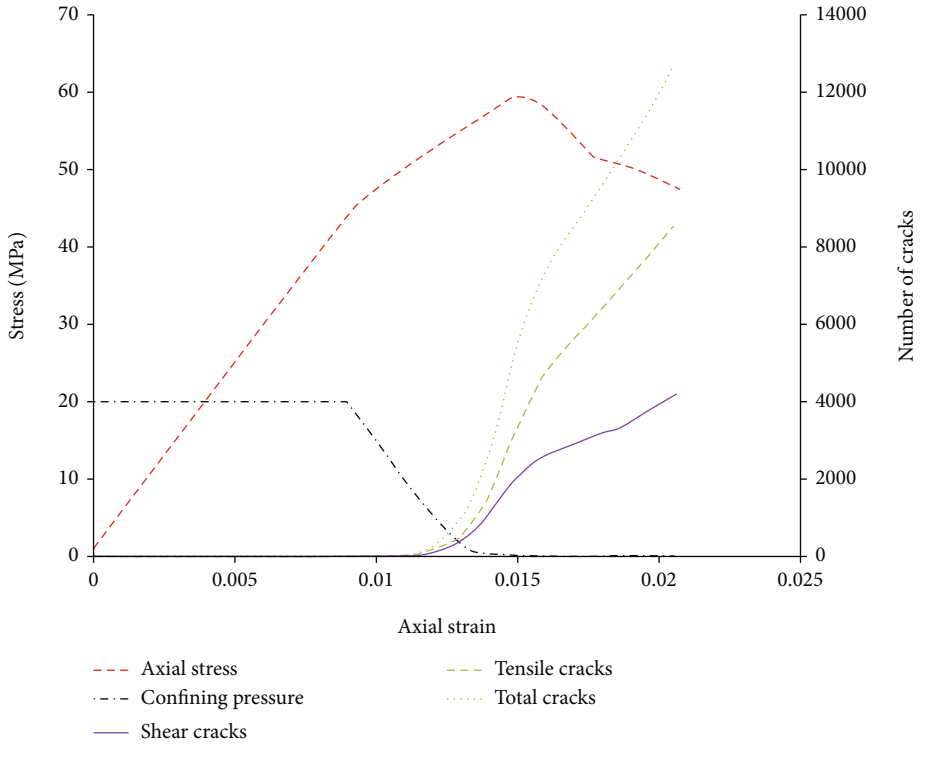

(b) 20 MPa

Figure 7: Continued.

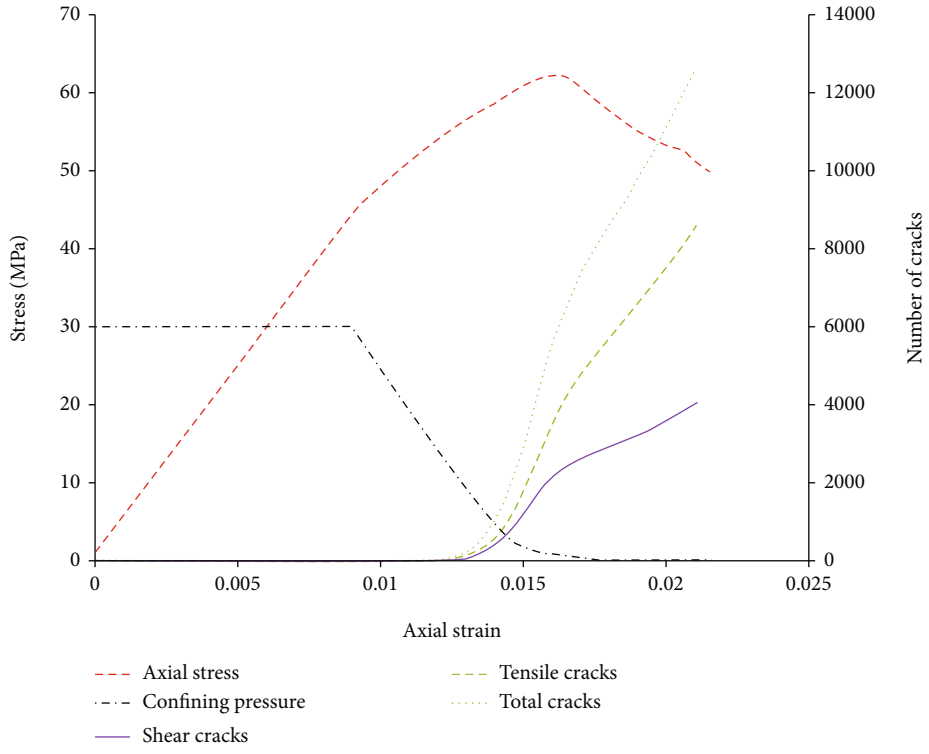

(c) 30 MPa

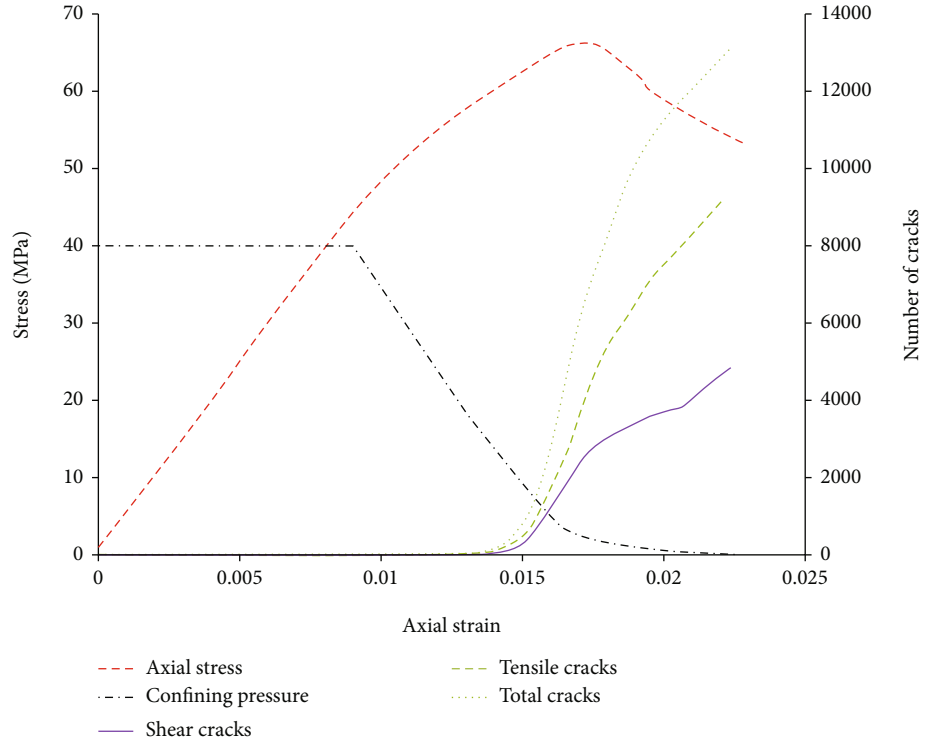

(d) 40 MPa

Figure 7: the relationship between stress-strain curves and cracks.

Figure 7 shows the relationship between stress-strain curves and cracks in the process of rock fracture under different confining pressures.

Figure 7 shows that under different confining pressures, almost no cracks occur in the rock before the axial stress reaches 0.8 times the peak stress; when the confining pressure is close to zero, there are many

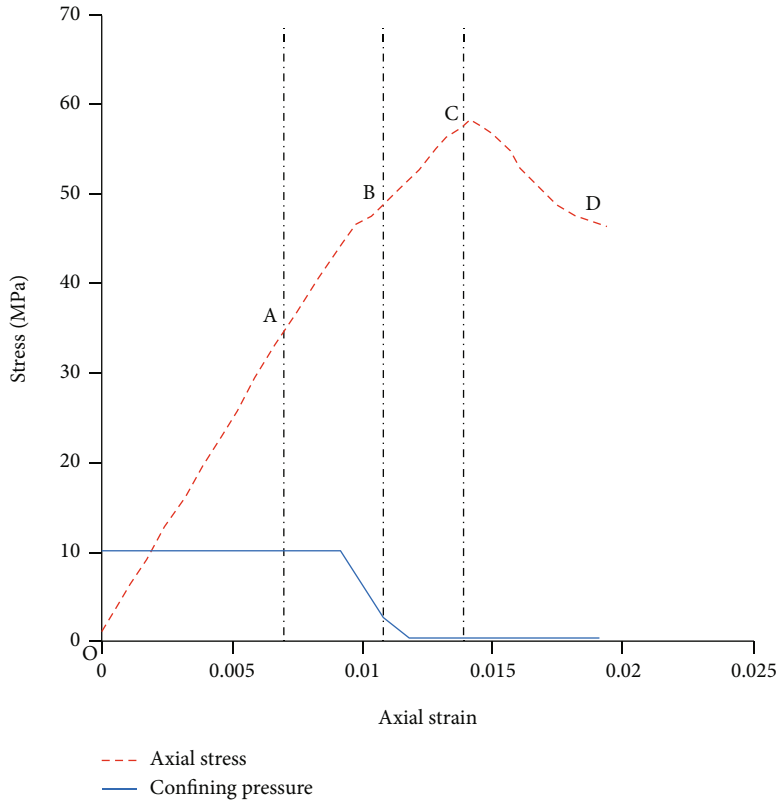

Figure 8: division of rock unloading failure stages.

cracks in the rock; the greater the confining pressure, the earlier the time when the rock begins to produce obvious cracks; when unloading failure occurs under different confining pressures, the growth rate of tensile cracks is obviously higher than that of shear fractures, and the number of tensile fractures is about twice that of shear fractures.

In conclusion, rock burst failure often occurs before confining pressure unloading is completed in high in situ stress areas. During rock burst, the tensile cracks account for about 70% of all fractures, and the unloading rock burst is a mixed failure of tensile and shear cracks.

In order to analyze the AE features of rock during confining pressure unloading well, the confining pressure of 10 MPa was taken as an example, the unloading deformation and failure process of rock was divided into four stages using the stress-strain curve and cracks propagation (see Figure 8).

As shown in Figure 8, in the stage OA, the internal cracks of the specimen are compacted, the strain energy is gradually accumulated, and there are no obvious cracks in the specimen; in the stage AB, the axial pressure continues to increase while the confining pressure of the specimen is unloaded, and the specimen gradually begins to produce obvious cracks; in the stage BC, when the axial pressure of the specimen continues to increase and the confining pressure unloading is close to zero, more cracks begin to appear. As the confining pressure is completely unloaded and the axial pressure continues to increase, a large number of cracks begin to appear; in the stage CD, the specimen is damaged and many cracks are then produced.

In the process of AE simulation using PFC, the moment tensor M_{ij} is the sum of the product of the contact force variation of each element related to the rupture and its distance to the AE event center [13]. The calculation expression of M_{ij} is as follows:

$$M_{ij} = \sum_{k=1}^{S} \Delta F_i^k R_j^k, \tag{1}$$

where ΔF_i^k is the ith component of the contact force change value; R_j is the j_{th} component of the distance between contact point and AE event center; S represents the number of particles in contact with the particle in which the rupture occurred.

Considering the large amount of memory needed to store the full distance tensor, the maximum scalar moment M_0 is used as the moment tensor for each AE event. The calculation expression of M_0 is as follows:

$$M_0 = \sqrt{\sum_{j=1}^{3} \frac{m_j^2}{2}}, \tag{2}$$

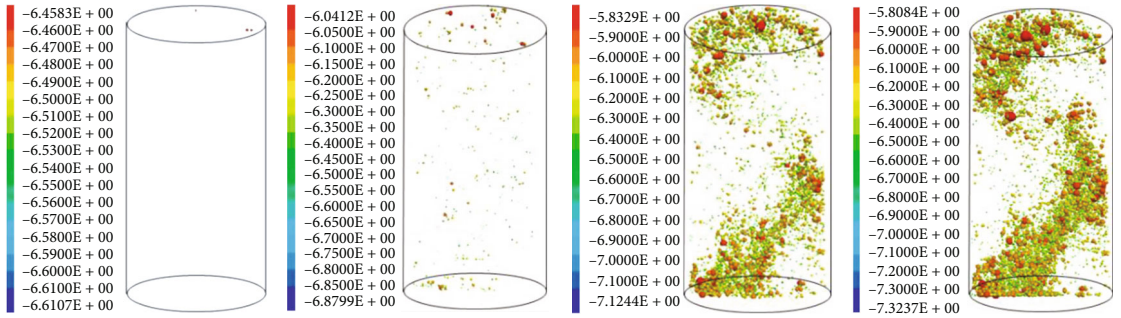

(a1) (a2) (a3) (a4)

(a) 10 MPa

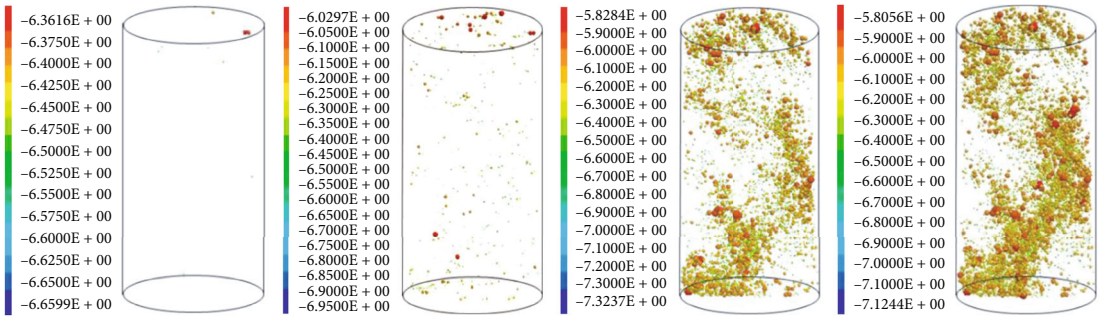

(b1) (b2) (b3) (b4)

(b) 20 MPa

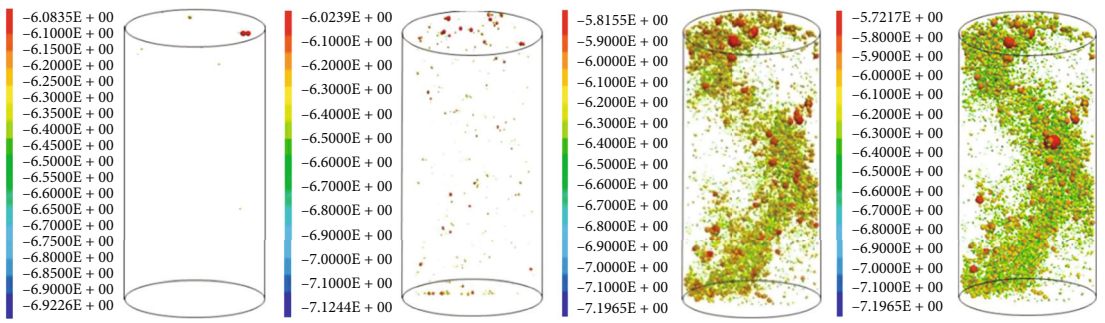

(c1) (c2) (c3) (c4)

(c) 30 MPa

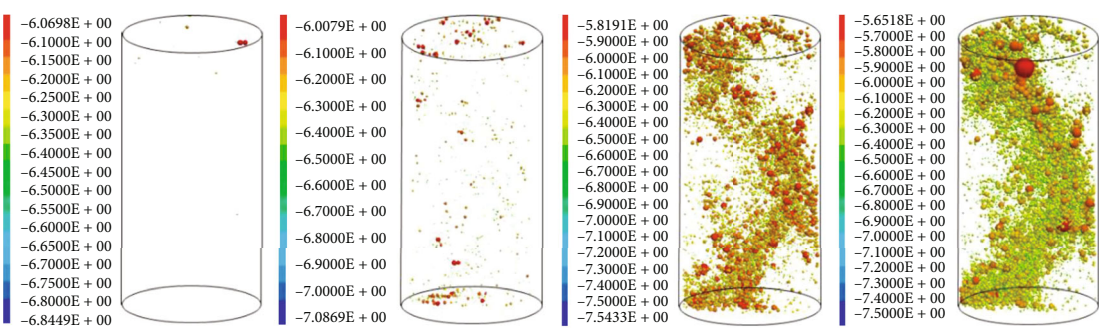

(d1) (d2) (d3) (d4)

(d) 40 MPa

Figure 9: AE position various at stages under different confining pressures.

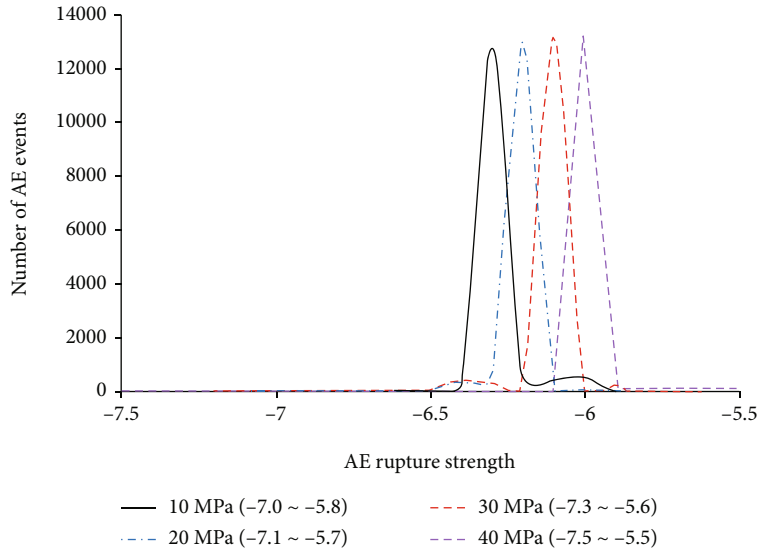

Figure 10: Relationship between AE rupture strength and the number of AE events.

where M_0 is the jth eigenvalue of the moment tensor matrix, $j = 1,2,3$.

The AE rupture strength M during rock fracture was determined by the following formula.

$$M = \frac{2}{3} \lg M_0 - 6. \tag{3}$$

Figure 9 shows the locations of AE in different failure stages under different confining pressures. The color and size of the balls in the figure reflect the size of AE rupture strength. The larger the ball, the redder the color, the greater the strength of AE rupture.

It can be seen from Figure 9 that under different confining pressures, the location expansion law of AE events is basically consistent in the process of rock confining pressure unloading failure; stage OA, there are almost no AE events in rocks, and only a few AE events appear at the top of the rock; stage AB, AE events of rock begin to appear at the top and bottom and expand rapidly from the top and bottom to the middle of the specimen, respectively; stage BC, the specimen reaches the peak stress, the specimen forms an obvious fracture zone, and a large number of AE events occur; stage CD, the specimen is damaged, and the AE rupture strength is mainly concentrated at the top and middle of the specimen; the greater the confining pressure, the greater the AE rupture strength of rock.

In conclusion, when rock burst damage occurs in tunnel rock face, cracks may rapidly expand from the top and bottom to the middle, and the locations of rock burst are mainly concentrated in the middle and top.

Under different confining pressure conditions, the relationship between AE rupture strength and the number of AE events during rock unloading failure is shown in Figure 10.

Figure 10 shows that AE rupture strength ranges from -7.5 to -5.5 in the process of rock failure under different confining pressures; with the increase of confining pressure, the AE rupture strength increases and the range of AE rupture strength expands; in the process of rock failure under different confining pressures, the AE rupture strength mainly concentrates in the range of -6.5~-6.0, and the ratio of the number of AE events to the total number of AE events exceeds 0.8, indicating that in the process of rock burst, the rock rupture strength is relatively concentrated and the number of AE events surge obviously.

4. Discussion

(1) In the process of rock mesoscopic rupture simulation, if each contact rupture between particles was regarded as an AE event, each AE rupture strength was consistent, which was inconsistent with the actual rock rupture. Therefore, when the initiation time and space of microcracks were similar, the occurrence of these microcracks was regarded as an AE event. In this way, a single AE event in rocks may not only produce one crack but also multiple cracks. Furthermore, the failure propagation velocity of the rock particle flow model under external load was half of the rock shear wave velocity [25], then the AE event duration could be calculated. The time from the moment when a microcrack was generated to the moment when the shear wave, caused by the microcrack, propagates to the inner boundary of the microcrack action area was recorded as T, and the AE event duration was 2 T. During the AE event duration, if there is no new microcrack in the action region of the microcrack, then the AE event contains a microcrack, while if there is a new microcrack, the microcracks are considered to belong to the same AE event, and the duration is recalculated and extended. According to the above method, the number of AE events during rock rupture was counted

(2) In order to study the crack initiation and propagation of rock under the rock burst stress path, the simulation results in this paper (Figure 7) were compared with similar test results [26]. The similarities and differences between the two results were then briefly described below

(a) The results of simulation and experiment show that there are few cracks before the peak stress in the process of confining pressure unloading, mainly internal bonding rupture, and a large number of cracks occur in the postpeak stage. The macroscopic fracture of rock is a combination of tension-shear

(b) For the test results, when the confining pressure is small, the tensile cracks first appear on the side edge of the specimen, and there are more tensile cracks during the failure process, while when the confining pressure is large, the shear cracks first appear in the middle of the specimen, and there are fewer tensile cracks during the failure process; for the simulation results, the tensile cracks first appear on the side edge and top of the specimen, and there are slightly more tensile cracks than shear cracks in the failure process

In conclusion, the simulation results are similar to the test results in terms of rock failure form and fracture generation time, but there are great differences in the spatial location of fracture generation and the ratio of shear cracks to tensile cracks. This may be because rocks with different in situ stress levels and types often have different structural features and thus exhibit different failure features. Furthermore, the mineral content and distribution of rocks as well as the original microfractures may also affect the initiation and expansion of cracks during the failure process.

5. Conclusions

In this work, the granite of the Lalin railway tunnel was taken as an example, and a particle flow model of the rock was established based on PFC^{3D} (three-dimensional particle flow code). The microscopic mechanical parameters of the particle flow model were calibrated using the results of uniaxial compression tests; the stress path of rock burst occurrence was simulated using the movement of walls in the particle flow model; acoustic emission (AE) features of the rock failure process under different confining pressures were then analyzed. It shows that:

(1) The rock burst numerical simulation results show that obvious radial deformation and strong dilatation deformation of rocks are caused by tunnel excavation; the greater the confining pressure, the faster the transformation of volumetric strain from compression to expansion, and the greater the possibility of rock burst in surrounding rock

(2) When unloading failure of the rock occurs under different confining pressures, the growth rate of the number of tensile cracks is significantly higher than that of shear cracks, and the number of tensile cracks is about twice that of shear cracks, which indicates that the tensile cracks generated during unloading rock burst failure of tunnel rock face account for about 70% of all cracks, and unloading rock burst failure is a mixed failure of tension and shear dominated by tension

(3) Under different confining pressures, the AE rupture strength mainly was concentrated between -6.5 and -6.0, the ratio of the number of AE events to the total number of AE events exceeds 0.8, which shows that the rock rupture strength is relatively concentrated and the surge of AE events is obvious in the process of rock burst

Data Availability

The data used to support the findings of this study are available from the corresponding author upon request.

Conflicts of Interest

The authors declare that they have no conflicts of interest.

Acknowledgments

Financial supports for the study were provided by the Natural Sciences Foundation Committee of China under Grant No. 41472254.

References

[1] D. Ma, H. Y. Duan, J. X. Zhang, X. W. Liu, and Z. H. Li, "Numerical simulation of water–silt inrush hazard of fault rock: a three-phase flow model," *Rock Mechanics and Rock Engineering*, vol. 55, no. 8, pp. 5163–5182, 2022.

[2] D. Ma, J. J. Wang, X. Cai et al., "Effects of height/diameter ratio on failure and damage properties of granite under coupled bending and splitting deformation," *Engineering Fracture Mechanics*, vol. 220, article 106640, 2019.

[3] D. Li, F. Zhao, and M. Zheng, "Fractal characteristics of cracks and fragments generated in unloading rockburst tests," *International Journal of Mining Science and Technology*, vol. 24, no. 6, pp. 819–823, 2014.

[4] B. Z. Tian, S. J. Liu, J. Li, P. Liang, Y. B. Zhang, and Z. L. Wang, "Experimental investigations into the effects of lithology on acoustic emission," *Journal of Engineering Science and Technology Review*, vol. 8, no. 3, pp. 210–216, 2015.

[5] Y. B. Zhang, G. Y. Yu, B. Z. Tian, X. X. Liu, and P. Liang, "Identification of multiple precursor information of acoustic emission dominant frequency in the process of granite failure," *Journal of Mining and Safety Engineering*, vol. 23, no. 2, pp. 355–362, 2017.

[6] G. S. Su, W. Gan, S. B. Zhai, and G. F. Zhao, "Acoustic emission precursors of static and dynamic instability for coarse-grained hard rock," *Journal of Central South University*, vol. 27, no. 10, pp. 2883–2898, 2020.

[7] F. Pei, H. G. Ji, J. W. Zhao, and J. M. Geng, "Energy evolution and AE failure precursory characteristics of rocks with different rockburst proneness," *Advance in civil engineering*, vol. 2020, article 8877901, 12 pages, 2020.

[8] S. B. Zhai, G. S. Su, S. D. Yin, S. Z. Yan, Z. F. Wang, and L. B. Yan, "Fracture evolution during rockburst under true-triaxial loading using acoustic emission monitoring," *Bulletin of Engineering Geology and the Environment*, vol. 79, no. 9, pp. 4957–4974, 2020.

[9] C. Q. Chu, S. C. Wu, Z. S. Cao, C. J. Zhang, and Y. L. Zhang, "Experimental research on fracture characteristics of granite with acoustic emission technology," *Journal of Central South University (Science and Technology)*, vol. 52, no. 8, pp. 2919–2932, 2021.

[10] C. L. Wang, C. Cao, Y. B. Liu, C. F. Li, G. Y. Li, and H. Lu, "Experimental investigation on synergetic prediction of rockburst using the dominant-frequency entropy of acoustic emission," *Natural Hazards*, vol. 108, no. 3, pp. 3253–3270, 2021.

[11] J. N. Tan, B. Wang, T. Feng, Y. Ning, B. B. Liu, and F. J. Zhao, "Acoustic emission characteristics of anchored sandstone under uniaxial compression and its correlation with rockburst," *Journal of Central South University (Science and Technology)*, vol. 52, no. 8, pp. 2828–2838, 2021.

[12] X. J. Wang, H. Zhang, Q. L. Chen, Q. Zeng, and J. Liu, "Acoustic emission characteristics and damage model of limestone loading with different rockburst tendencies," *Chinese Journal of Rock Mechanics and Engineering*, vol. 41, no. 7, pp. 1373–1383, 2019.

[13] Y. Zhou, S. C. Wu, X. L. Xu, W. Sun, and X. P. Zhang, "Particle flow analysis of acoustic emmision characteristics during rock failure process," *Chinese Journal of Rock Mechanics and Engineering*, vol. 32, no. 5, pp. 951–959, 2013.

[14] J. F. Cai, S. C. Wu, Y. T. Gao, Y. Zhou, Y. H. Gao, and X. Q. Huang, "Rock failure mechanism under uniaxial compression condition based on P-T diagram of moment tensors," *Journal of China University of Mining and Technology*, vol. 45, no. 3, pp. 500–506, 2016.

[15] Z. Zhang, G. Wang, Y. J. Jiang et al., "Acoustic emission characteristics and failure mechanism of fractured rock under different loading rates," *Shock and Vibration*, vol. 2017, Article ID 5387459, 13 pages, 2017.

[16] H. J. Wang, F. Zhao, Z. Q. Huang, H. C. Yu, J. R. Niu, and P. Zhang, "Study on acoustic emission characteristics of sandstone under different fracture modes," *Arabian Journal of Geosciences*, vol. 11, no. 24, p. 772, 2018.

[17] Y. F. Wang, W. X. Yang, H. Z. Jiao, L. P. Wang, and H. B. Zhao, "Simulation of acoustic emission and damage properties of granite in brittle and ductile failure processes," *Journal of Yangtze River Scientific Research Institute*, vol. 77, no. 33, pp. 76–80, 2016.

[18] W. R. Liu, W. Yuan, Y. T. Yan, and X. Wang, "Analysis of acoustic emission characteristics and damage constitutive model of coal-rock combined body based on particle flow code," *Symmetry*, vol. 11, no. 8, p. 1040, 2019.

[19] W. G. Gao, H. Q. Duan, and Y. X. Yang, "Particle flow simulation of acoustic emission characteristics of coal and rock under periodic loading," *Chinese Journal of Applied Mechanics*, vol. 38, no. 1, pp. 262–268, 2021.

[20] W. R. Liu, J. K. Liu, and C. Zhu, "Multi-scale effect of acoustic emission characteristics of 3D rock damage," *Arabian Journal of Geosciences*, vol. 12, no. 22, pp. 1–13, 2019.

[21] Z. L. Feng, X. Chen, Y. Fu, S. S. Qing, and T. G. Xie, "Acoustic emission characteristics and joint nonlinear mechanical response of rock masses under uniaxial compression," *Energies*, vol. 14, no. 1, p. 200, 2021.

[22] J. Z. Hu, Y. J. Wang, Z. M. Ma, X. G. Ma, X. Y. Zhang, and G. Y. Yu, "Experimental and numerical analysis of rock burst tendency and crack development characteristics of Tianhu granite," *Geofluids*, vol. 2021, Article ID 6681261, 12 pages, 2021.

[23] *National Standards Compilation Group of People's Republic of China. GB 50287-2016 Code for Hydropower Engineering Geological Investigation*, China Planning, Beijing, 2016.

[24] D. Y. Huang, J. M. Xu, and T. Chen, "Calibration of microscopic mechanical parameters of granite using actual distributions and orthogonal simulations," in *Proceedings of the 7th International Conference on Discrete Element Methods. DEM 2016*, X. Li, Y. Feng, and G. Mustoe, Eds., vol. 188 of Springer Proceedings in Physics, pp. 935–943, Springer, Singapore, 2017.

[25] R. Madariaga, "Dynamics of an expanding circular fault," *Bulletin of the Seismological Society of America*, vol. 66, no. 3, pp. 639–666, 1976.

[26] B. X. Wang, A. B. Jin, Y. Q. Zhao et al., "Strength characteristics and 3D fracture evolution law of granite under unloading confining pressure," *Journal of Harbin Institute of Technology*, vol. 52, no. 11, pp. 137–146, 2020.